*Geophys. J. Int.* (1999) **137,** 747–754

# *SV*-wave azimuthal anisotropy in the Australian upper mantle: preliminary results from automated Rayleigh waveform inversion

E. Debayle

*Research School of Earth Sciences, Australian National University, Canberra* ACT 0200, *Australia. E-mail: eric@rses.anu.edu.au*

Accepted 1999 January 7. Received 1999 January 5; in original form 1998 December 15

## SUMMARY

The pattern of azimuthal anisotropy for *SV* waves in the upper mantle beneath Australia has been determined using a two-stage tomographic procedure for Rayleigh waves. The inversion exploits an automated procedure based on the waveform inversion method of Cara & Lévêque (1987) to allow the analysis of 668 vertical-component seismograms within a few weeks. The automated procedure provides an effective choice of the secondary observables used in the waveform inversion for both fundamental and higher modes, allowing the construction of a set of radially stratified upper-mantle models which represent the average structures on paths criss-crossing the Australian continent. The 668 path-average models are then combined in a 3-D velocity model which describes the lateral variation of the *SV* velocity and its azimuthal anisotropy. The lateral variations in wave speed show a good overall agreement with previous results for shear wave-speed variations in Australia but are accompanied by significant azimuthal anisotropy. At 150 km depth the anisotropy displays a simple pattern with most of the directions of fast *SV* velocities dominated by a north–south component close to the present-day absolute plate motion. Nevertheless, in the regions with the highest shear wave speed, anisotropy is not aligned with the current plate motion, suggesting a local resistance to mantle flow.

**Key words:** anisotropy, surface waves, tomography, waveform inversion.

## 1 INTRODUCTION

In the last 15 years, large improvements have been made in mapping the upper mantle with surface wave data. Higher modes have been incorporated in surface wave analysis, which allows an increase in depth resolution (e.g. Lerner Lam & Jordan 1983; Cara & Lévêque 1987; Nolet 1990; Stutzmann & Montagner 1993; van Heijst & Woodhouse 1997). The lateral resolution in global tomographic models has increased, with structure now available on scale lengths of 1000 km (e.g. Trampert & Woodhouse 1996). However, if one wishes to obtain results directly relevant to current geodynamic problems such as the scale length of mantle convection or the detection of small objects such as hotspots, a finer lateral resolution is required. This can be supplied by supplementing permanent stations with temporary networks of broad-band recorders.

Such experiments have recently taken place in the southwest Pacific islands (Pillet *et al.* 1999), but the most significant improvements have been shown to be possible in continental areas. In Australia, the SKIPPY experiment (van der Hilst *et al.* 1994) has been designed to exploit the high regional seismicity surrounding the continent. Using an array of a few portable instruments, a large volume of regional seismograms has been collected in a relatively short time. Rayleigh wave seismograms recorded during this experiment have been analysed by Zielhuis & van der Hilst (1996) and van der Hilst *et al.* (1998) using the partitioned waveform inversion of Nolet (1990).

The Cara & Lévêque (1987) method (hereafter designated as CL) offers an alternative for waveform inversion of regional seismograms. The approach has been designed to minimize the dependence on the starting model. This is very helpful in developing an automated procedure which aims to match the waveforms of large volumes of individual records, starting with synthetic seismograms computed with a single upper-mantle model.

This paper outlines an automated procedure based on the work of CL, as well as presenting the first results of a successful application to upper-mantle structure in three dimensions beneath Australia. As in Nolet (1990), the structure is retrieved using a two-stage procedure, but different algorithms are used at each step of the process. First, automated waveform inversion is employed to find a path-averaged 1-D radially stratified upper-mantle model compatible with the waveform of each individual seismograms. Second, the continuous regionalization scheme of Montagner (1986) is applied to the path-averaged models to retrieve local structure. At this stage, the analysis is confined to the fundamental and first higher modes of Rayleigh wave seismograms, but the inversion

© 1999 RAS

has produced a 3-D model of *SV* wave-speed variation and azimuthal anisotropy beneath the Australian region.

## 2 WAVEFORM INVERSION USING SECONDARY OBSERVABLES: AN AUTOMATED PROCEDURE

The waveform of the surface wave portion of a seismogram is well known to depend in a highly non-linear way on the elastic parameters. Nolet (1990) used a non-linear optimization technique to minimize the difference between synthetic and real waveforms. In the CL method, the non-linearity of the inverse problem is reduced by using a set of secondary observables built up from the waveforms as the prime data of the inversion. As in Lerner Lam & Jordan (1983), the contribution of a given mode in the output signal is reinforced by cross-correlation techniques, but the non-linearity is reduced by using secondary observables based on the amplitude of the envelope of these cross-correlogram functions. The CL approach, which is close to the isolation filter technique of Gee & Jordan (1992), allows a 1-D depth-dependent model compatible with the waveform of a surface wave seismogram to be found after a few iterations of a linearized inversion scheme.

In this section, I focus on how the CL method can be automated. First a strategy is proposed for automatic selection of the secondary observables and then the outline of the automated waveform inversion procedure is presented.

### 2.1 Automatic selection of the secondary observables

The secondary observables introduced in the CL technique are extracted from the observed and a complete synthetic seismogram by cross-correlation with synthetic seismograms for individual modes computed for a reference model. The resulting cross-correlogram functions are then bandpass filtered around different frequencies. The combination of bandpass filtering and cross-correlation can be represented as

$$g_p(\omega_q, t) = h(\omega_q, t) * s(t) * \check{s}_p(-t)\,. \tag{1}$$

Here $*$ denotes a convolution, $h(\omega_q, t)$ is the impulse response of a bandpass filter centred on the circular frequency $\omega_q$, $s(t)$ denotes the observed seismogram, $\hat{s}_p(t)$ is a pure mode synthetic signal computed for mode branch $p$ for a reference model, and $\check{s}_p$ denotes the complex conjugate of $\hat{s}_p$. The actual secondary observables used by CL are defined by sampling three values taken at different time lags on the envelope of the modal cross-correlogram functions $g_p(\omega_q, t)$, with a visual inspection of the envelope. One value is taken on the appropriate maximum of the envelope and two others on either side of this position. The inversion seeks to minimize the difference between these actual secondary observables and those computed for a complete synthetic seismogram $\hat{s}(t) = \Sigma(\hat{s}_p(t))$. The instantaneous phase of the cross-correlogram, taken at the time where the envelope reaches its maximum, is generally also included to adjust the waveform fit.

An example is presented in Fig. 1 which summarizes the situation before inversion for the 1994 August 22 event located at (11.62°S; 166.46°E) and recorded at station SC08 (−22.27°S; 131.37°E) during the third SKIPPY deployment. For this intermediate-depth event (150 km), a dominant fundamental mode is observed between 3.5 and 4 km s$^{-1}$ on the actual signal (lower part of the figure), while the less energetic overtones have higher group velocities. The initial synthetic seismogram resembles the actual signal, but is slightly delayed compared to the real data. On the upper part of the figure, the envelopes of the actual cross-correlogram functions filtered at 40 s have several maxima corresponding to different alignments of the cross-correlated signals. For mode 0 (see Fig. 1), the actual seismogram is cross-correlated with the fundamental mode of the reference synthetic seismogram. Note that a single model is used both as reference and initial model, so that the reference synthetic seismogram is the same as the initial synthetic. The largest maximum is found in the centre of the diagram, close to the reference time $t_0 = 0$, for which their is no delay between the two signals. This is due to the small difference in arrival time between the fundamental mode of the synthetic and actual signals. For modes 1 to 4, the actual seismogram is cross-correlated with the overtones of the reference synthetic seismograms. The energetic fundamental mode still dominates the amplitude of the envelope, but the corresponding lobe is found on the border of the diagram, at a larger delay time corresponding to the delay between the fundamental mode of the actual seismogram and the overtones of the synthetic. The less energetic overtones of the actual seismogram produce secondary lobes close to the time $t = 0$ because the reference model gives a good prediction of the arrival time of the overtone.

Fig. 1 illustrates the potential ambiguity in an automated sampling of actual cross-correlogram functions. The modal cross-correlogram functions can have a complex shape with several maxima, especially when several energetic modes interfere in the seismograms. An intuitive choice would be to sample the three points on the largest maximum of each actual envelope. Experience shows that when a mode $j$ is clearly dominant in the actual signal (e.g. the fundamental mode for a shallow event) it is likely to contaminate the $g_p(\omega_q, t)$ functions and to provide the largest maximum of the envelope even when $p \neq j$. In this case, by selecting the largest maximum, redundant information on the dominant mode $j$ is introduced in the inverse problem, while the information on the other modes is lost. An alternative would be to select the closest maximum with respect to the reference time $t_0 = 0$, where the maximal energy for the considered mode is expected, if the two cross-correlated signals are not delayed. This supposes a good reference model which predicts well the arrival times on the actual seismogram. In practice, several maxima are often found close to $t_0 = 0$ for most of the envelopes, which introduces ambiguity in the automated sampling.

As an automated selection of the pertinent maximum will always be ambiguous, the strategy adopted in this study is to overparametrize the cross-correlation information. This could be done by inverting for each point of the envelope of the cross-correlogram, which will increase the computation time by adding redundant information, but ensure a complete coverage of all the details of the waveform. The danger is then succeeding in matching the noise as well as the signal. A compromise has been preferred: each lobe is represented by three values (taken on the maximum of the lobe and on either side of the central peak) as in the original CL method, but when the shape of the envelope has several maxima, several lobes are selected. For the 1994 August 22 earthquake (Fig. 1), two lobes of the cross-correlograms filtered at 40 s have been sampled by three values. The secondary observables are thus selected according to the following criteria.

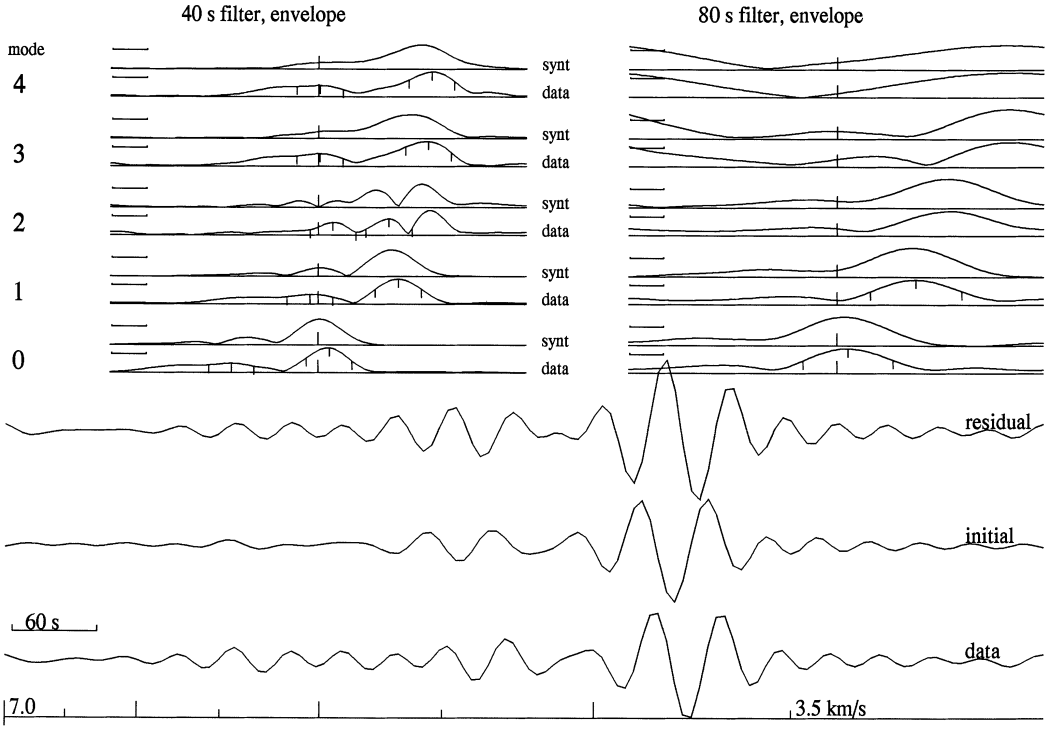


**Figure 1.** The 1994 August 22 event recorded at the SKIPPY station SC08, situation before inversion. The lower part of the figure shows: (1) the observed seismogram (labelled 'data') (2) the synthetic seismogram computed for the initial model ('initial') and (3) their difference ('residual'). The upper part of the figure shows the envelopes of the filtered cross-correlogram functions $g_p(w_q, t)$ for modes $p$ ranging from 0 (fundamental mode) to 4 (fourth overtone) and for filters centred on 40 (left column) and 80 s (right column) periods. For each mode and each period, the lower functions are the cross-correlograms between the pure-mode synthetics and the data and the upper functions are the cross-correlograms with the complete synthetic seismogram. The vertical bar in the centre of each diagram corresponds to the reference time $t_0 = 0$ (see text). Vertical marks indicate the points where the actual envelopes are sampled for the inversion. In the CL method, three values are sampled after a visual check on the pertinent lobe of the actual envelope. In the automated process, the cross-correlation information is overparametrized by allowing several lobes to be sampled.

(1) First, all the significant maxima of the envelope are extracted. A maximum is considered to be significant when the ratio $R_1$ between the amplitude of the maximum and the average of the minima of the envelope is greater than a threshold value (3 in this study).

(2) If several maxima are extracted, the two best are selected, using the ratio $A_{\max}/|t_{\max} - t_0|$ as a criterion, where $A_{\max}$ is the amplitude of the maximum, $t_{\max}$ the time at which the maximum is found and $t_0$ the reference time.

(3) The instantaneous phase of the cross-correlogram is taken at the maximum with the highest $A_{\max}/|t_{\max} - t_0|$ ratio.

This compromise has proven to be effective. The approach favours the largest lobes close to the reference time $t_0$, where the current mode is expected, and when the choice between two lobes is ambiguous, both are selected. Such a choice allows the information contained in each mode to be taken into account, without adding a large volume of redundant data.

## 2.2 Outline of the procedure

Once the automatic selection of the secondary observables has been implemented, a workable automated procedure can be developed. The automated algorithm analyses all the data in sequence, according to the following procedure.

The synthetic seismogram is computed for the given earthquake and epicentre–station path. The source parameters are taken from the NEIS catalogue and the stress–displacement functions needed to compute the source excitation functions are computed using the information provided by the 3-D *a priori* model 3SMAC (Nataf & Ricard 1995) in the epicentre region. The initial and reference model for the upper mantle is a smoothed PREM model (Dziewonski & Anderson 1981). The crust is averaged along each path within the 3SMAC model. If the synthetic does not predict the amplitude of the real seismogram within a factor of 5, the seismogram is rejected as this poor amplitude prediction is likely to be attributed to a poor knowledge of the source parameters or to departures from ray theory.

The central frequencies $\omega_q$ of the bandpass filter $g_p(\omega_q, t)$ have to be chosen. A maximum of three periods in the frequency range 40–160 s are selected by comparing the amplitude of the envelope of the signal $A_s$ (part of the record arriving with a group velocity larger than 3.3 km s$^{-1}$) to the amplitude of the envelope of the noise $A_n$ (part of the record arriving with a group velocity smaller than 3.3 km s$^{-1}$) at the following periods: 40, 80, 160 s and 40, 60, 120 s. A particular period is considered for use in the waveform inversion when $A_s/A_n$ is larger than a threshold value (3 in this study), and the central frequencies of the bandpass filter are chosen according to the following sequence of priorities:

(1) 40, 80, 160 s;
(2) 40, 60, 120 s;
(3) 40, 80 s;
(4) 40, 60 s.

A minimum frequency range (40–60 s) is thus imposed in the analysis of the waveform data. At 60 s period, the use of a filtered cross-correlogram is sufficient to constrain the *SV* velocity to a depth greater than 250 km, even when only the fundamental mode is taken into account in the inversion (Lévêque *et al.* 1991).

The waveform inversion is broken up into four steps. In the first step the actual envelopes filtered at 'long period'; that is, periods larger than 40 s are matched. The envelopes at 'short period' (i.e. 40 s) are included as a second step, once the lower-frequency envelopes have been matched. The third step consists of adding the instantaneous phase of the filtered cross-correlograms at 60 or 80 s depending on the central frequency chosen for the 'long period' envelopes. Finally, as a fourth step, the phase at short period is added. This strategy is a very efficient way to avoid phase skips of $2\pi$. The inversion of the envelope for the whole frequency range can be seen as an indirect way to obtain an elastic model which explains the group velocity of the different mode branches of the seismogram. Starting from this elastic model, the instantaneous phase at low frequency is added, where $2\pi$ phase shifts are not to be expected, before moving towards higher frequencies. This approach is close to that followed by van Heijst & Woodhouse (1997) but the inversion is not separated mode by mode. At a given frequency, all those modes which contribute more than 1 per cent of the total energy of the initial synthetic seismogram are considered in the inversion.

Finally, several conditions have to be fulfilled in order to progress through the different steps of the waveform inversion. At the end of the first and second steps the misfit parameter $\chi_d^2$ is computed:

$$\chi_d^2 = \frac{1}{n}\sum_i \left(\frac{\hat{d}_i - d_{ci}}{\sigma_i}\right)^2, \tag{2}$$

where $n$ is the number of data, $\hat{d}_i$ the data $i$ (secondary observable), $d_{ci}$ the calculated data and $\sigma_i$ the standard deviation for the data $i$, together with the data variance reduction in the step. The process is allowed to start the following step only if $\chi_d$ is small or if the variance reduction is large.

At the end of the fourth and last step, the inversion is considered successful if the following hold.

(1) The final model provides a good fit to the actual seismogram. I use the following measures of fit:

$$E_{res/act} = E_{resfin}/E_{actual}$$

and an energy reduction parameter

$$Re = (E_{resinit} - E_{resfin})/E_{resinit},$$

where $E_{resfin}$ and $E_{resinit}$ are the energy of the residual signal at the final and initial iterations and $E_{actual}$ is the energy of the actual signal. These energies are summed over the signal for group velocities between 3.5 and 6 km s$^{-1}$. The result is accepted if $E_{res/act}$ is smaller than 0.3 or if $Re$ is larger than 90 per cent.

(2) The algorithm has converged towards a unique model. I use the following criterion:

$$S = \chi_m(i) - \chi_m(i-1),$$

where $\chi_m^2$ is the quadratic perturbation of the model and $i$ is the current iteration of the process. If the variation in $S$ is weak (smaller than 0.05) between the two last iterations, the result is considered to be stable.

Fig. 2 shows the situation after the successful application of the automated process to the 1994 August 22 earthquake. The instantaneous phase of the filtered cross-correlograms at 80 and 40 s has been added in the last steps of the process. A good fit to the data has been obtained ($\chi_d = 0.99$), which can be seen in Fig. 2 by comparing the actual and synthetic cross-correlogram functions. The fit to the actual seismogram is also very good, with $E_{res/act} = 0.09$, and the energy reduction parameter $Re$ reaches 94 per cent. A small residual signal remains within the variability associated with the standard deviation attributed to the data (see Section 3).

## 3 APPLICATION TO THE AUSTRALIAN CONTINENT: PRELIMINARY RESULTS

For this application, I have used Rayleigh wave seismograms recorded mainly during the SKIPPY experiment, complemented by data collected during a deployment of eight broad-band stations in the Kimberley, West Australia from July to October 1997 and by a few data recorded at the permanent IRIS station NWAO.

I have chosen to work with an inversion in terms of *SV* wave speed, attenuation parametrized by $\log(Q)$ and the scalar moment through $\log(M_0)$. The covariance matrices employed in the inversion follow the approach of Lévêque *et al.* (1991) with standard deviations adapted to the parametrization used in this study. I use a value of 0.05 km s$^{-1}$ for the *SV* velocity, 0.25 for $\log(Q)$ and 0.5 for $\log(M_0)$. The standard deviation on the envelope data is taken as 10 per cent for those lobes when the ratio $R_1$ (as defined in Section 2.1) is larger than 6 and 30 per cent when $3 < R_1 < 6$. The phase data are always taken for the envelope with 10 per cent error and its standard deviation is fixed to 5 per cent of $2\pi$ radians.

The automated procedure applied to these Rayleigh wave data with this set of *a priori* choices has resulted in 668 path-averaged models corresponding to the path coverage shown in Fig. 3. At this stage, a dense distribution of paths has been obtained for central and eastern Australia. However, significant improvements are still possible by adding data recorded over a longer period of time on the permanent IRIS and GEOSCOPE stations in the Australasian region. In this paper, the potential of the automated procedure is illustrated with a striking, but robust geophysical result of this preliminary inversion. In a subsequent paper, a detailed discussion of a complete tomographic model including the GEOSCOPE and IRIS data will be presented.

A preliminary tomographic map for the lateral variation in *SV* wave velocity and its anisotropy is shown at a depth of 150 km in Fig. 4. This image has been obtained by continuous regionalization (Montagner 1986) of the path-averaged velocity models using the theoretical framework described in Lévêque *et al.* (1998) for the inversion of the azimuthal anisotropy. Lateral variations in *SV* wave speed are represented

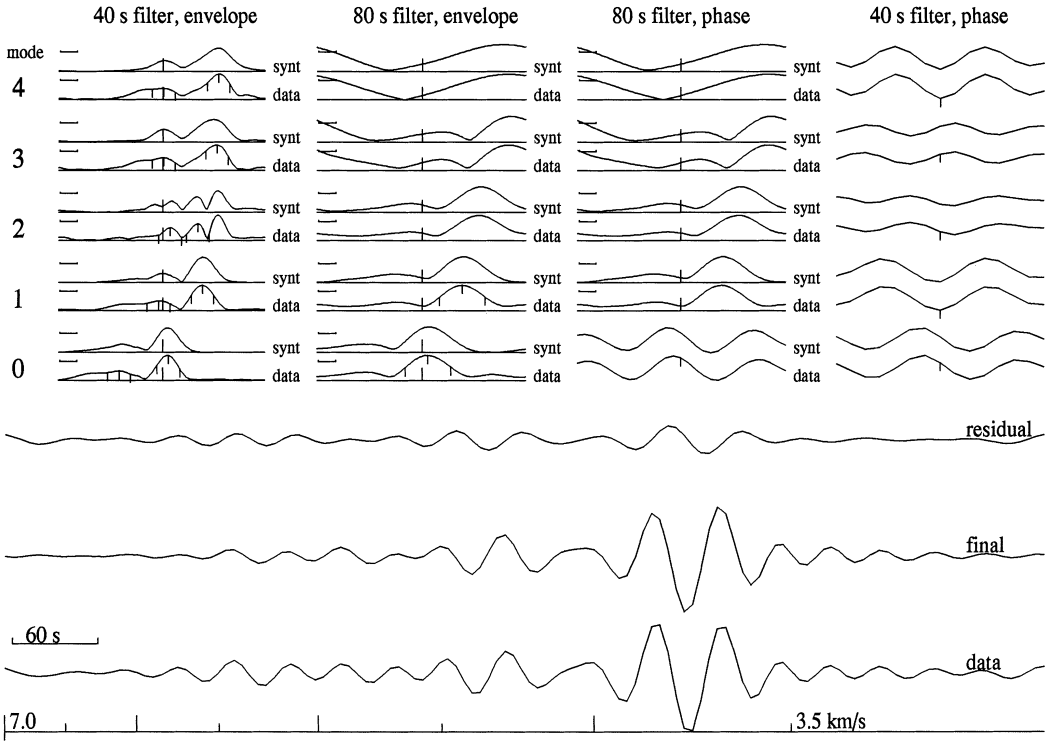


**Figure 2.** As Fig. 1, but after inversion using the automated process. The instantaneous phase of the filtered cross-correlograms at 80 and 40 s has been added in the last step of the process (the two right columns in the upper part of the figure).

in colour while azimuthal anisotropy is displayed with bars showing the directions of maximum velocity for an *SV* wave propagating horizontally. The length of the bars is proportional to the peak-to-peak azimuthal anisotropy expressed as a percentage of the shear wave speed. The average value is around 1 per cent for Australia with a maximum just below 3 per cent on the eastern margin of the continent. The main feature of the map in Fig. 4 is a simple pattern of anisotropy with a dominant north–south direction for most of the Australian plate. This simple pattern is not observed at shallower depths, where a complex organization with abrupt changes in the fast *SV* directions dominates. In addition, lateral variations in *SV* wave speed show a general agreement with the previous studies of Zielhuis & van der Hilst (1996)

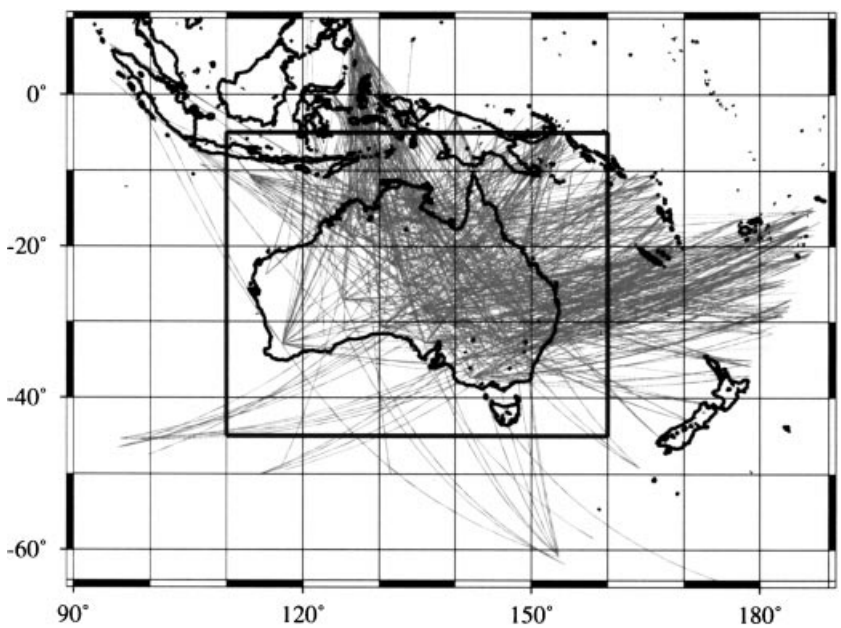


**Figure 3.** Rayleigh wave path coverage used in this study. The box shows the area for which the map in Fig. 4 is displayed.

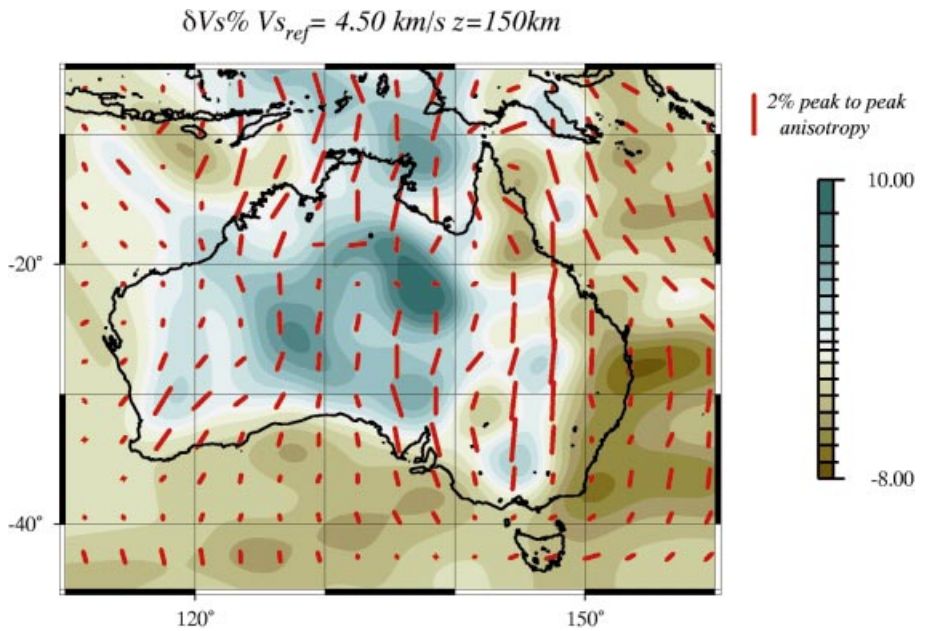


**Figure 4.** Map view at 150 km depth of the lateral variation in azimuthal anisotropy and shear wave speed. Velocity contrasts (per cent) are represented by colours; fast directions of horizontally propagating *SV* waves are represented by bars. The western part of Australia (west of 125°E) is not well resolved in this study.

and van der Hilst *et al.* (1994). Low velocities are found on the eastern Phanerozoic margin of the continent, whilst west of 140°E the Precambrian cratons which characterize central Australia are underlain by higher seismic velocities.

Before discussing the geophysical results presented here, their robustness is addressed. First, the lateral smoothness of the map presented in Fig. 4 is constrained by a horizontal correlation length $L_{\mathrm{corr}}$, which defines the width of a Gaussian *a priori* function on the model. For *SV* heterogeneities, $L_{\mathrm{corr}}$ should be chosen in order that the 'effective' section of the paths with width $L_{\mathrm{corr}}$ ensure a good coverage of the area under study (Montagner 1986). For *SV* wave azimuthal anisotropy, a variation depending on $2\theta$ is expected, where $\theta$ is the azimuth of the path (e.g. Montagner & Nataf 1986). Such a variation can be sampled only if a minimum of three paths with different azimuths are present in each cell of width $L_{\mathrm{corr}}$. After several trials, I have chosen a correlation length of 200 km for both the *SV* wave speed and the azimuthal anisotropy. This choice favours a smooth model for central and eastern Australia, where a large density of crossing paths is available. This can be seen in Fig. 4, where the pattern of seismic wave speed heterogeneity is characterized by horizontal wavelengths of the order of 400 km, larger than the wavelengths of the Rayleigh waves for the longest period considered. Such a smooth model has the advantage of minimizing contamination by effects not considered in the theory, such as diffraction by lateral heterogeneities or mislocation of the epicentres. However, due to a large redundancy in the data set, a somewhat low variance reduction of 70 per cent is obtained at 150 km depth. Other values of $L_{\mathrm{corr}}$ were tried for both *SV* heterogeneities and azimuthal anisotropy, resulting in a slightly smoother or rougher pattern of heterogeneities and anisotropy, but the results discussed here are not affected by reasonable changes in $L_{\mathrm{corr}}$.

A second important question concerns the significance of azimuthal anisotropy. A first partial answer is obtained by performing an isotropic inversion, allowing only for lateral variations in *SV* wave speed. The result is a velocity field similar to the one observed in Fig. 2 but with a substantial increase in the amplitude of seismic heterogeneities, reaching 1.35 per cent in some parts of the map. Thus, when anisotropy is not allowed in the inversion, part of the anisotropic signal is incorporated in the *SV* velocity field to contribute to improved data fit. For this reason, the introduction of azimuthal anisotropy allows a limited improvement in the data fit of at least 4 per cent in variance reduction. I have also tried to reduce the isotropic correlation length in order to map azimuthal anisotropy in short-wavelengths seismic heterogeneities. With a value of $L_{\mathrm{corr}}$ of 100 km for *SV* heterogeneities, the amplitude of anisotropy does not decrease and the directions are not changed.

Thus, a small amount of anisotropy is present at 150 km depth, even when short-wavelength heterogeneities are allowed in the model. This level of anisotropy can be removed if substantial increases in the amplitude of *SV* heterogeneities are allowed, with the consequence of a reduction in the level of data fit. When anisotropy is included in the parametrization, the anisotropic directions cannot be changed, whatever the *a priori* chosen for the model. Finally, it should be noted that the north–south pattern of anisotropy observed in Fig. 4 is smooth over distances of thousands of kilometres, much larger than the correlation lengths adopted in this study. If short-wavelength variations are required by the data, they appear in the model, as can be seen in Fig. 4 beneath the North Australian craton, where anisotropy becomes weak or east–west. Thus, the simple north–south pattern is a feature of the model required by the data, not imposed by the *a priori* assumptions. A final question concerns the importance of higher modes in constraining the structure at 150 km depth. Of the 668 paths of this study, higher modes have been considered in the inversion for 393 paths. For the periods considered in this study, the use of the cross-correlogram information for the

fundamental mode alone is sufficient to constrain the structure at 150 km depth (see Section 2.2), and the higher modes provide additional information.

Most works on continental anisotropy have employed observations of teleseismic *SKS* splitting. Because this class of data provides poor constraints on the depth location of the anisotropic layer, continental anisotropy has either been interpreted as mainly frozen in the lithosphere (Silver & Chan 1991) or as a primary effect of recent plate motion movements (Vinnik *et al.* 1992). This controversy has been illustrated by recent regional studies in continental areas. Barruol *et al.* (1997) argue for 'fossil' lithospheric anisotropy beneath the cratonic core of the North American craton, with a possible asthenospheric flow around the cratonic keel. For South Africa, Vinnik *et al.* (1995) interpreted their splitting measurements for the Kaapvaal craton as observations of shearing of the mantle by the plate above. In Australia, *SKS* measurements for the Precambrian cratons have been attributed to a crustal fabric but do not entirely rule out the presence of deeper anisotropy (Clitheroe & van der Hilst (1998). On the eastern margin of the continent, where *SKS* measurements suggest a deeper origin, the observed directions may results from the superposition of two anisotropic layers with different fast-axis azimuths (Girardin & Farra 1998).

In this work, the pattern of anisotropic directions represented in Fig. 4 is constrained at a depth of 150 km by the dispersion of Rayleigh waves. In addition, the directions of fast *SV* waves obtained would correspond to the *a*-axis of olivine crystals. Assuming an olivine-dominated mineralogy, the pattern of fast directions can thus be plausibly interpreted in terms of the azimuth of shear strain responsible for crystal orientation. The smooth pattern of anisotropy displayed in Fig. 4 is clearly not compatible with short-wavelength lithospheric deformations. Large-scale processes have thus to be invoked in the mantle. With the agreement between our anisotropic directions and the northward movement of the Australian plate, the most likely candidate is shearing of the mantle by the plate above. The results presented here thus support the evidence presented by Vinnik *et al.* (1995) that the old continental roots that lie below 150 km depth must be deformed by plate motion. Other evidence for a north–south flow beneath Australia comes from a previous regional surface wave study of the Indian Ocean (Lévêque *et al.* 1998). From a tomographic procedure similar to the one used in this paper, but applied to a much poorer data set for Australia, these authors found a north–south anisotropic direction at 200 km depth, a larger depth than this study. However, as noted by Lévêque *et al.* (1998), their north–south direction is mainly constrained by one piece of data, a north–south path analysed only at periods larger than 60 s (Debayle 1996), which provides a poorer vertical resolution than the 40 s data used in this study. A small vertical smearing, compatible with the vertical correlation length of 50 km used in the Indian ocean study (Debayle & Lévêque 1997), can explain the shift at depth of the north–south anisotropic layer found by Lévêque *et al.* (1998). Vinnik *et al.* (1992) noted that the threshold temperature at which the mobility of olivine is sharply enhanced would correspond to a depth somewhat less than 150 km for Precambrian cratons. Frozen anisotropy is thus unlikely to be preserved over long periods of time below 150 km depth, supporting the anisotropy directions related to recent plate motion observed in this study.

Finally, it should be noted that the results presented in this paper are not inconsistent with other anisotropic measurements beneath Australia. As mentioned above, *SKS* measurements available for central Australia do not rule out the presence of lithospheric or asthenospheric anisotropy, while on the eastern margin of the continent, measurements may be biased by the presence of several anisotropic layers. Gaherty & Jordan (1995) proposed a model for paths crossing the northern and western parts of Australia with anisotropy in the uppermost 250 km of the mantle. Tong *et al.* (1994) indicated the presence of an anisotropic layer located below 210 km for northern Australia, but their data set did not allow them to place constraints on the shallower part of their model.

The evidence presented in this paper favours the existence of large-scale deformation in the continental mantle due to plate motion. Present-day deformation is observed at 150 km depth beneath most of the Precambrian mantle of central Australia. However, in the North Australian craton, where the highest seismic wave speed are observed, anisotropy is either weak or east–west. This suggests a local resistance to mantle flow in the thickest part of the craton, a hypothesis that will be tested in a following paper, involving a larger data set.

## ACKNOWLEDGMENTS

I would like to thank B. L. N. Kennett, J. J. Lévêque, L. Rivera and M. Cara for fruitful discussions at various stages of this work. I also thank the IRIS team for providing data at NWAO and the members of RSES who participated in the collection of the Skippy and Kimba data in the field. Figs 3 and 4 were made using the GMT software package.

## REFERENCES

Barruol, G., Silver, P.G. & Vauchez, A., 1997. Seismic anisotropy in the eastern United States: deep structure of a complex continental plate, *J. geophys. Res.,* **102,** 8329–8348.

Cara, M. & Lévêque, J.J., 1987. Waveform inversion using secondary observables, *Geophys. Res. Lett.,* **14,** 1046–1049.

Clitheroe, G. & van der Hilst, R.D., 1998. Complex anisotropy in the Australian lithosphere from shear-wave splitting in broad-band *SKS* records, in *Structure and Evolution of the Australian Continent,* eds Braun, J., Dooley, J., Goleby, B., van der Hilst, R. & Klootwijk, C., *AGU Geodyn. Ser.,* **26,** 73–78.

Debayle, E., 1996. Tomographie du manteau supérieur de l'Océan Indien par inversion de forme d'ondes, *Thèse de Doctorat,* Université Louis Pasteur, Strasbourg.

Debayle, E. & Lévêque, J.J., 1997. Upper mantle heterogeneities in the Indian Ocean from waveform inversion, *Geophys. Res. Lett.,* **24,** 245–248.

Dziewonski, A.M. & Anderson, D.L., 1981. Preliminary reference earth model, *Phys. Earth planet. Inter.,* **25,** 297–356.

Gaherty, J.B. & Jordan, T., 1995. Lehmann discontinuity as the base of an anisotropic layer beneath continents, *Science,* **268,** 1468–1471.

Gee, L.S. & Jordan, T.H., 1992. Generalized seismological data functionals, *Geophys. J. Int.,* **111,** 363–390.

Girardin, N. & Farra, V., 1998. Azimuthal anisotropy in the upper mantle from observations of *P*-to-*S* converted phases: application to southeast Australia, *Geophys. J. Int.,* **133,** 615–629.

Lerner Lam, A.L. & Jordan, T.H., 1983. Earth structure from fundamental and higher modes analysis, *Geophys. J. R. astr. Soc.,* **75,** 759–797.

Lévêque, J.J., Cara, M. & Rouland, D., 1991. Waveform inversion of surface wave data: test of a new tool for systematic investigation of upper mantle structures, *Geophys. J. Int.,* **104,** 565–581.

Lévêque, J.J., Debayle, E. & Maupin, V., 1998. Anisotropy in the Indian ocean upper mantle from Rayleigh- and Love-waveform inversion, *Geophys. J. Int.,* **133,** 529–540.

Montagner, J.P., 1986. Regional three-dimensional structures using long-period surface waves, *Ann. Geophys.,* **4,** 283–294.

Montagner, J.P. & Nataf, H.C., 1986. A simple method for inverting the azimuthal anisotropy of surface waves, *J. geophys. Res.,* **91,** 511–520.

Nataf, H.C. & Ricard, Y., 1995. 3SMAC: an *a priori* tomographic model of the upper mantle based on geophysical modeling, *Phys. Earth planet. Inter.,* **95,** 101–122.

Nolet, G., 1990. Partitioned waveform inversion and two dimensional structure under the network of autonomously recording seismographs, *J. geophys. Res.,* **95,** 8499–8512.

Pillet, R., Rouland, D., Roult, G. & Wiens, D.A., 1999. Crust and upper mantle heterogeneities in the southwest Pacific from surface wave phase velocity analysis, *Phys. Earth planet. Inter.,* **110,** 211–234.

Silver, P.G. & Chan, W.W., 1991. Shear wave splitting and subcontinental mantle deformation, *J. geophys. Res.,* **96,** 16 429–16 454.

Stutzmann, E. & Montagner, J.P., 1993. An inverse technique for retrieving higher mode phase velocity and mantle structure, *Geophys. J. Int.,* **113,** 669–683.

Tong, C., Gudmundsson, O. & Kennett, B.L.N., 1994. Shear wave splitting in refracted waves returned from the upper mantle transition zone beneath northern Australia, *J. geophys. Res.,* **99,** 15 783–15 797.

Trampert, J. & Woodhouse, J.H., 1996. High resolution global phase-velocity distributions, *Geophys. Res. Lett.,* **23,** 21–24.

van der Hilst, R., Kennett, B., Christie, D. & Grant, J., 1994. Skippy: mobile broad-band arrays to study the seismic structure of the lithosphere and mantle beneath Australia, *EOS, Trans. Am. geophys. Un.,* **75,** 177, 180–181.

van der Hilst, R.D., Kennett, B.L.N. & Shibutani, T., 1998. Upper-mantle structure beneath Australia from portable array deployment, in *Structure and Evolution of the Australian Continent,* eds Braun, J., Dooley, J., Goleby, B., van der Hilst, R. & Klootwijk, C., *AGU Geodyn. Ser.,* **26,** 39–57.

van Heijst, H.J. & Woodhouse, J.H., 1997. Measuring surface-wave overtone phase velocities using a mode-branch stripping technique, *Geophys. J. Int.,* **131,** 209–230.

Vinnik, L.P., Makeyeva, L.I., Milev, A. & Usenko, A.Yu., 1992. Global patterns of azimuthal anisotropy and deformations in the continental mantle, *Geophys. J. Int.,* **111,** 433–447.

Vinnik, L.P., Green, R.W.E. & Nicolaysen, L.O., 1995. Recent deformations of the deep continental root beneath southern Africa, *Nature,* **375,** 50–53.

Zielhuis, A. & van der Hilst, R.D., 1996. Upper-mantle shear velocity beneath eastern Australia from inversion of waveforms from SKIPPY portable arrays, *Geophys. J. Int.,* **127,** 1–16.